Journal of Alloys and Compounds 741 (2018) 1258–1268

Contents lists available at ScienceDirect

Journal of Alloys and Compounds

journal homepage: http://www.elsevier.com/locate/jalcom

A novel photocatalytic water splitting solar-to-hydrogen energy conversion: Non-centro-symmetric borate $CsZn_2B_3O_7$ photocatalyst

A.H. Reshak

New Technologies - Research Centre, University of West Bohemia, Univerzitni 8, 306 14 Pilsen, Czech Republic

ARTICLE INFO

Article history:
Received 18 September 2017
Received in revised form
15 January 2018
Accepted 16 January 2018
Available online 31 January 2018

Keywords:
Ultraviolet photocatalyst
Borate $CsZn_2B_3O_7$
DFT
Non-centro-symmetric

ABSTRACT

The photocatalytic performance of the novel borate $CsZn_2B_3O_7$ is theoretically investigated by means of density functional theory. The calculation highlights that the packing of the BO_3 structural unit is the main source for the large macroscopic photophysical properties in $CsZn_2B_3O_7$ due to high anisotropic electron distribution. The potentials of the conduction band (CB) and valence band (VB) edges values of $CsZn_2B_3O_7$ are −1.789 eV and 3.891 eV, respectively. The CB edge potential of $CsZn_2B_3O_7$ is more negative than the redox potential of H^+/H_2, indicating that the $CsZn_2B_3O_7$ has strong reduction power for H_2 production. The absorption edge of $CsZn_2B_3O_7$ occurs at $\lambda = 218$ nm and the optical band gap is estimated to be 5.68 eV, in good agreement with the experimental data (5.69 eV). Therefore, $CsZn_2B_3O_7$ expected to be an efficient photocatalyst in the ultraviolet (UV) region. Thus, $CsZn_2B_3O_7$ possesses an appropriate band gap width and suitable CB edge position together, which leads to a higher efficiency of light-driven photocatalytic H_2 production. Also, it possesses high photogenerated carrier mobility and high electronic conductivity, which favors the enhancement of the photocatalytic performance. The large photocatalytic performance is due to the strong interactions between the ZnO_4 tetrahedra and co-parallel BO_3 triangle groups. In this study we provide a detailed investigation concerning the suitability of $CsZn_2B_3O_7$ to be used as an efficient photocatalyst under UV irradiation utilizing the first-principle material approaches, which greatly improves the search efficiency and greatly helps experiments to save resources in the exploration of new photocatalysts with good photocatalytic performance.

1. Introduction

The search for novel photocatalysts, materials with promising structural and photocatalytic performance, is still a challenge for scientists. To produce efficient photocatalytic performance, the materials should possess high mobility carriers, suitable band gap width and, hence, good absorption capacity [1,2]. A balance between the light absorption capacity and the reduction power in the investigated material leads to a higher efficiency of light-driven photocatalytic H_2 production [3,4]. The other important requirement is, the photocatalysts must show efficient separation and migration ability of the photoexcited carriers, due to the fact that the photocatalytic reaction utilizes the photoexcited electrons (e^-) and holes (h^+) migrating to the surface of the photocatalyst. The photocatalysis process doesn't produce any pollutants because it uses photon energy and water and, hence, it will make a great contribution to energy and environmental challenges in the near future. Also, the high-performance photocatalyst system requires low recombination of photogenerated e^- and h^+ to ensure that the reduction and oxidation reactions can occur favorably in the conduction band (CB) and valence band (VB) of a semiconductor photocatalyst [5]. However, it remains challenging to efficiently design a suitable high-performing photocatalyst material.

It was reported that in borate materials, the large electronegativity difference between B and O atoms is very favorable for transmittance of short-wavelength light [6]. In general, the B and O atoms in borates form planer triangles $(BO_3)^{3-}$ and $(BO_4)^{5-}$ polyhedra. The BO_3 groups can adopt a coplanar configuration promoting efficient absorption capacity. In BO_3 groups, three O atoms are linked with a B atom, eliminating three dangling bonds of the BO_3 groups, which further widens its transparency in the UV region. Moreover, the high anisotropic electron distribution in BO_3 groups favors the enhancement of the absorption capacity [7]. Therefore, searching for novel photocatalyst materials able to produce efficient photocatalytic performance in visible and UV regions has attracted a great deal of research in recent years. Good

E-mail address: maalidph@yahoo.co.uk.

https://doi.org/10.1016/j.jallcom.2018.01.227
0925-8388/

examples are studies of $KBe_2BO_3F_2$ (KBBF) and $Sr_2Be_2B_2O_7$ (SBBO) single crystals [8–11], which could generate efficient photocatalytic performance in the UV region but, due to the high toxicity of the beryllium oxide powders, it remains challenging to safely grow crystals of large size. To overcome the drawback of the high toxicity, substitution of Zn for Be is suggested to eliminate the toxicity issues inherent in the synthesis of KBBF and SBBO from beryllium oxide powders. Therefore, introducing the new $CsZn_2B_3O_7$ single crystal opens the ability to safely grow crystals and increase the efficiency of the photocatalytic performance almost to double in borate crystals due to the presence of the distorted $(ZnO_4)^{6-}$ tetrahedra. Moreover, the introduction of the Zn atom causes red-shift to the absorption edge of $CsZn_2B_3O_7$ to 218 nm [6]. Thus, we addressed ourselves to investigate the influence of $(ZnO_4)^{6-}$ tetrahedra on the crystal structure and, hence, on the resulting photocatalytic performance. The packing of the BO_3 structural unit may also affect the macroscopic structure [12] and, hence, the photocatalytic performance. The large absorption capacity is due to the strong interactions between the cations and co-parallel BO_3 triangle groups [12]. The novelty and the aim of this work is to provide a qualitative and quantitative investigation to report reliable photocatalytic performance from $CsZn_2B_3O_7$.

Because it is still desirable to find materials with promising photocatalytic properties, the search for a better candidate has not ceased. Therefore, we provide a detailed depiction of the electronic structure, transport, photocatalytic and optical properties of $CsZn_2B_3O_7$ using the full-potential method, which is timely and will bring us important insights into understanding the origin of the band structure, density of states, photocatalytic and photophysical properties. Hence, it is very important to use a full-potential method based on the density functional theory (DFT). It is well known that the DFT approaches have the ability to accurately predict the ground state properties of materials, and the developed analytic tools are vital to investigating their intrinsic mechanism. This microscopic understanding has further guided molecular engineering design for new materials with novel structures and properties. It is anticipated that first-principle material approaches will greatly improve the search efficiency and greatly help experiments to save resources in the exploration of new crystals with good performance [13–27]. For instance, several researchers have used the first-principles calculation to explore new photocatalysts and found good agreement with the experimental results [22–34]. We would like to mention that, in our previous work [28–34], we calculated the energy band gaps and the photophysical properties using the full-potential method for several systems whose energy band gaps and photophysical properties are known experimentally, and a very good agreement with the experimental data was obtained. Thus, we believe that our calculations reported in this paper will produce very accurate and reliable results which will greatly help experiments to save resources in the exploration of new photocatalysts with good photocatalytic performance.

2. Computational details

The photocatalytic performance of the newly synthesized $CsZn_2B_3O_7$, with sixteen formula units per unit cell crystallizing in a $Cmc2_1$ orthorhombic space group [8,35], is theoretically investigated by means of density functional theory. It was reported that $CsZn_2B_3O_7$ is isostructural to $KBe_2BO_3F_2$ (KBBF) [10,11], $Sr_2Be_2B_2O_7$ (SBBO) [36–39] and $KBe_2B_3O_7$ [23], but with a larger optical response due to the presence of the distorted $(ZnO_4)^{6-}$ tetrahedra, and eliminates the toxicity issues from beryllium oxide powders and the red-shift of the absorption edge of $CsZn_2B_3O_7$. Fig. 1 shows the crystal structure of the newly synthesized $CsZn_2B_3O_7$, in which the BO_3 anionic groups exhibit a planar shape with conjugated

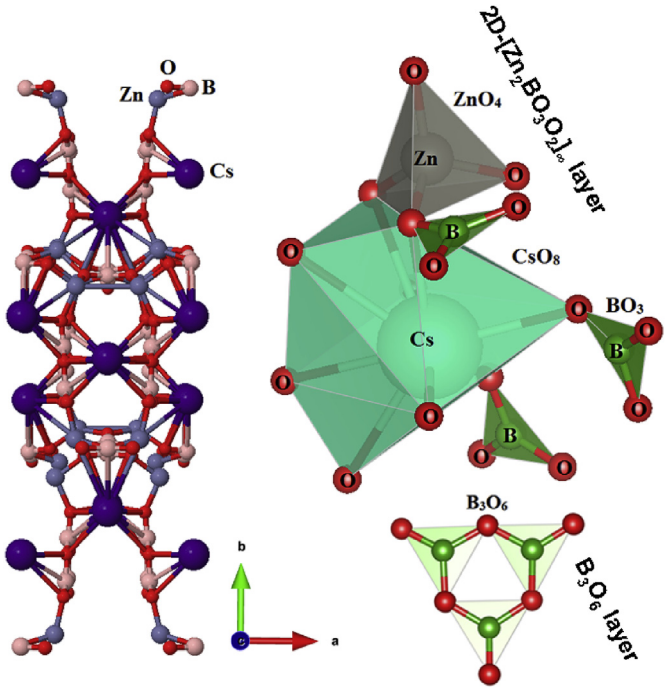

Fig. 1. The crystal structure of the newly synthesized $CsZn_2B_3O_7$.

electron orbitals, which make the BO_3 anionic groups the main source of the large optical properties in $CsZn_2B_3O_7$. The distorted $(ZnO_4)^{6-}$ tetrahedra are the main source to increase the efficiency of the optical absorbance. The B_3O_6 groups originate from the connection of three BO_3 triangles, in which only B3, B4 and B5 atoms participate in B_3O_6 groups, whereas B1, B2 and B6 atoms form ($B1O_3$, $B2O_3$ and $B6O_3$) isolated triangles. These isolated triangles adopt a nearly coplanar configuration, which enhances the optical absorbance in borate crystals. It is interesting to highlight that the BO_3 triangles in $CsZn_2B_3O_7$ are connected by ZnO_4 tetrahedra to form 2D-$[Zn_2BO_3O_2]_\infty$ layers (Fig. 1). Also three of the BO_3 triangles are connected to form 1D-B_3O_6 layers (Fig. 1). The structure of these layers is believed to be favorable to the formation of a self-built internal static electric field, which is very beneficial to the separation and migration of photoinduced e^- and h^+ [23,39].

To investigate the suitability of $CsZn_2B_3O_7$ to be used as an efficient photocatalyst, the experimental crystallographic data of $CsZn_2B_3O_7$ [35] are optimized using the all-electron full-potential method (wien2k code [40]) within the Perdew, Burke, Ernzerhof generalized gradient approximation (PBE-GGA) [41]. More details about the DFT calculation and level of theory are provided as supplementary materials. The optimized structure of $CsZn_2B_3O_7$ along with $[Zn_2BO_3O_2]_\infty$ and B_3O_6 layers are shown in Fig. 1. Using the recently modified Becke-Johnson potential (mBJ) [42], the resulting optimized geometrical structure is used to investigate the suitability of $CsZn_2B_3O_7$ to be used as an efficient photocatalyst. For this, the basis functions in the interstitial region are expanded up to $R_{MT} \times K_{max} = 7.0$ and inside the atomic spheres for the wave function. The $l_{max} = 10$ and the charge density is Fourier expanded up to $G_{max} = 12(\text{a.u.})^{-1}$. To obtain self-consistency, a mesh of 4000 $\vec{k}$ points in the irreducible Brillouin zone (IBZ) is used. The self-consistent calculations are converged, since the total energy of the system is stable within 0.00001 Ry. A mesh of 50000 $\vec{k}$ points in the IBZ is used to perform the calculation of the photophysical and photocatalytic properties. The input required for calculating the photophysical and photocatalytic properties are the energy

eigenvalues and eigenfunctions which are the natural outputs of band structure calculation.

3. Results and discussion

3.1. Structure-property relationship

Since $CsZn_2B_3O_7$ crystallizes in a non-centro-symmetric structure, it is very interesting to highlight that the non-centro-symmetric structure induces a spontaneous polarization due to the displacement of the center of the positive and negative charges in a unit cell [43]. Due to the fact that their positive and negative charges have different centers of symmetry, the non-centro-symmetric materials are among the ferroelectric materials that have a macroscopic polarization which induces the accumulation of charges at the surfaces [44]. Thus, a spontaneous polarization can be screened by free electrons (e^-) in the CB and free holes (h^+) in the VB, and/or by ions adsorbed on the surface from the solution forming a Stern layer [45]. A positive charge in positive fields is screened by external and internal mechanisms [46]. The internal mechanism forms a negatively charged region below the surface, and the external mechanism consists of the adsorption of foreign negatively charged ions at the surface, whereas the opposite reactions take place in negative fields, and the adsorbed foreign ions are positively charged. This charge reallocation generates an electric field around the charge region [47]. A polarization field is compensated for at equilibrium by the screening mechanisms. Thus, the photogenerated electrons can easily migrate to the surface and give rise to oxidation and reduction products at different locations [48–50]. This in turn enhances the photocatalytic activity. We should emphasizes that the unique photochemistry of the non-centro-symmetric materials may be utilized to launch some new photoreaction pathways.

The trigonal BO_3 anionic group possesses a conjugated π orbital which can be polarized easily. It is well known that BO_3 is one of the most active groups in non-centro-symmetric borate crystals [51]. Moreover, the B–O units possess strong electron cloud overlap and prefer to attract h^+ and repel e^-, thus facilitating separation of the photogenerated $e^- - h^+$ pairs. This in turn enhances the photocatalytic activity. It is interesting to highlight that the polarizability causes the potential energy of charged particles and transition states to lower regardless of whether these particles are negatively or positively charged [52].

To investigate the suitability of $CsZn_2B_3O_7$ to be used as an efficient photocatalyst, it is necessary to examine the electronic structure [53], since the photocatalytic performance is directly related to the electronic band structure and, hence, to the location of the top of valence bands (TVB) and the bottom of conduction bands (BCB). The electronic band structure along the high symmetry directions of the first BZ and the total density of states of $CsZn_2B_3O_7$ are calculated to explore the bands' dispersion and the nature of the fundamental energy band gap, and the locations of the TVB and BCB, as shown in Fig. 2(a). The photocatalytic oxidation of the materials is mainly attributed to the participation of superoxide radicals $(O_2^{\bullet-})$, hydroxyl radicals $(^{\bullet}OH)$ and photogenerated holes [54]. To understand the photocatalytic mechanism of $CsZn_2B_3O_7$, the reduction and oxidation potentials of the CB and the VB edges at the point of zero charge can be obtained following the equations given in Ref. [55]:

$$E_{CB} = \chi - E^C - (E_g/2) \quad (1)$$

$$E_{VB} = E_{CB} + E_g \quad (2)$$

where E_{CB} and E_{VB} are the potentials of CB and VB edges, respectively, E^C is the free energy corresponding to the hydrogen scale, and the value is ~4.5 eV [55], E_g and χ are the band gap and the electronegativity of semiconductors, respectively [55]. The E_{CB} and E_{VB} values of $CsZn_2B_3O_7$ are −1.789 eV and 3.891 eV, respectively Fig. 2(b). This Fig. 2(b) illustrates the probable energy level diagram (potential *vs.* NHE), displaying the relative positions of CB and VB for $CsZn_2B_3O_7$, and redox potentials for O_2/H_2O and H_2/H_2O. The downward shifted CB bottom lies below the redox potential of H_2/H_2O (0.0 eV), whereas the VB top lies above the O_2/H_2O redox potential (1.23 eV) [56]. For H_2 evolution, the CB of the photocatalyst must be more negative than the redox potential of H^+/H_2, and the reduction power depends on the position of the CB edge. Following Fig. 2(b), it can be clearly seen that the CB of $CsZn_2B_3O_7$ is more negative than the redox potential of H^+/H_2, indicating that the $CsZn_2B_3O_7$ has strong reduction power for H_2 production. Generally, an appropriate band gap width and suitable CB edge position together contribute to the optimal H_2 production activity under light irradiation. Therefore, a balance between the light absorption capacity and the reduction power in the investigated material leads to a higher efficiency of light-driven photocatalytic H_2 production. Thus, the second important factor for photocatalysts to be efficient is the band gap width and, hence, the absorption capacity. It has been reported that the substitution of Be by Zn causes a red-shift in the absorption edge of $CsZn_2B_3O_7$ to 218 nm [6] with respect to the absorption edge of its isostructural $KBe_2BO_3F_2$, $Sr_2Be_2B_2O_7$ and $KBe_2B_3O_7$ (144 nm) [8,9,35–39], which implies that the absorption edge of $CsZn_2B_3O_7$ occurs in the UV region. To confirm this, the absorption spectrum is calculated and presented in Fig. 2(c), which shows that $CsZn_2B_3O_7$ exhibits strong absorption at the level of $10^4\ cm^{-1}$.

In general, the absorption edge's value of the semiconductors can be clarified as follow: the square of the absorption coefficient, $[I(\omega)]^2$, is linear with energy (E) for direct optical transitions in the absorption edge region, whereas $[I(\omega)]^{1/2}$ is linear with E for indirect optical transitions [23,24]. Since the calculated electronic band structure of $CsZn_2B_3O_7$ confirms the direct nature of the band gap, the data plots of the $[I(\omega)]^2$ *vs.* E is linear in the absorption edge region, as shown in the inset of Fig. 2(c). Thus, the absorption edge of $CsZn_2B_3O_7$ is caused by direct transitions and the absorption edge occurs at $\lambda = 218$ nm, which corresponds to the optical band gap 5.68 eV, in good agreement with the experimental data (5.69 eV) [35]. One very important requirement is that the photocatalysts must show efficient migration ability of the photoexcited carriers, due to the fact that the photocatalytic reaction utilizes the photoexcited e^- and h^+ migrating to the surface of the photocatalyst. Therefore, the extinction coefficient, $K(\omega)$, as a function of photon energy is plotted and shown in Fig. 2(d and e). The extinction coefficient is directly proportional to the absorption coefficient, $I(\omega)$, i.e. shows a direct relation to the absorption of the material. The extinction coefficient shows the amount of loss of absorption when an electromagnetic wave passes through the material. It is represented by the following equation [57–59]:

$$I(\omega) = 4\pi K(\omega)/\lambda, \quad (3)$$

where λ is the wave length of light. Thus, the extinction coefficient obtained from equation (3) is given below [57–59]:

$$K(\omega) = I(\omega)\lambda/4\pi K. \quad (4)$$

Following Fig. 2(d and e), the extinction coefficient graph is increasing with energy to reach its maximum value of about 10.0 eV. At this energy limit, i.e. where the peaks are maximum, the compounds have the affinity to absorb more light. Furthermore, the

frequency-dependent optical conductivity Fig. 2(f) confirms that the absorption edge of the $CsZn_2B_3O_7$ occurs at 5.68 eV, corresponding to $\lambda = 218$ nm. The optical conductivity can be obtained from the complex first-order linear optical dielectric function following the expression $\varepsilon(\omega) = 1 + \frac{4\pi i\sigma(\omega)}{\omega}$, [58,59]. It consists of imaginary and real parts; therefore, it completely characterizes the linear optical properties.

In comparison, KBBF derivatives contain two types of B–O groups; one of the B–O groups consists of the coparallel BO_3 triangles. The second B–O group is located between the two adjacent $[Be_2BO_3O_2]$ and connects them together with an antiparallel arrangement, resulting in canceling their contribution to the macroscopic optical response. Hence, the optical responses in KBBF derivatives mainly arise from the coparallel BO_3 triangles. Therefore, the number density of the coparallel BO_3 triangles will determine the optical response of the KBBF [9–11]. In contrast, in $CsZn_2B_3O_7$, the B_3O_6 groups are located between adjacent $[Zn_2BO_3O_2]$ layers and are antialigned (Fig. 1). Thus, the optical response of $CsZn_2B_3O_7$ should also come from the coparallel BO_3 triangles, which was confirmed by Yu et al. [8]. They reported that the net dipole moment of the BO_3 triangles and $(ZnO_4)^{6-}$ tetrahedra are pointed along the polar c-axis, which means that BO_3 triangles and $(ZnO_4)^{6-}$ tetrahedra largely contribute to the optical response more than B_3O_6 groups [8]. Moreover, our investigation confirms that the $CsZn_2B_3O_7$ possesses a large optical response, considerable optical anisotropy, an absorption edge at $\lambda = 218$ nm and the

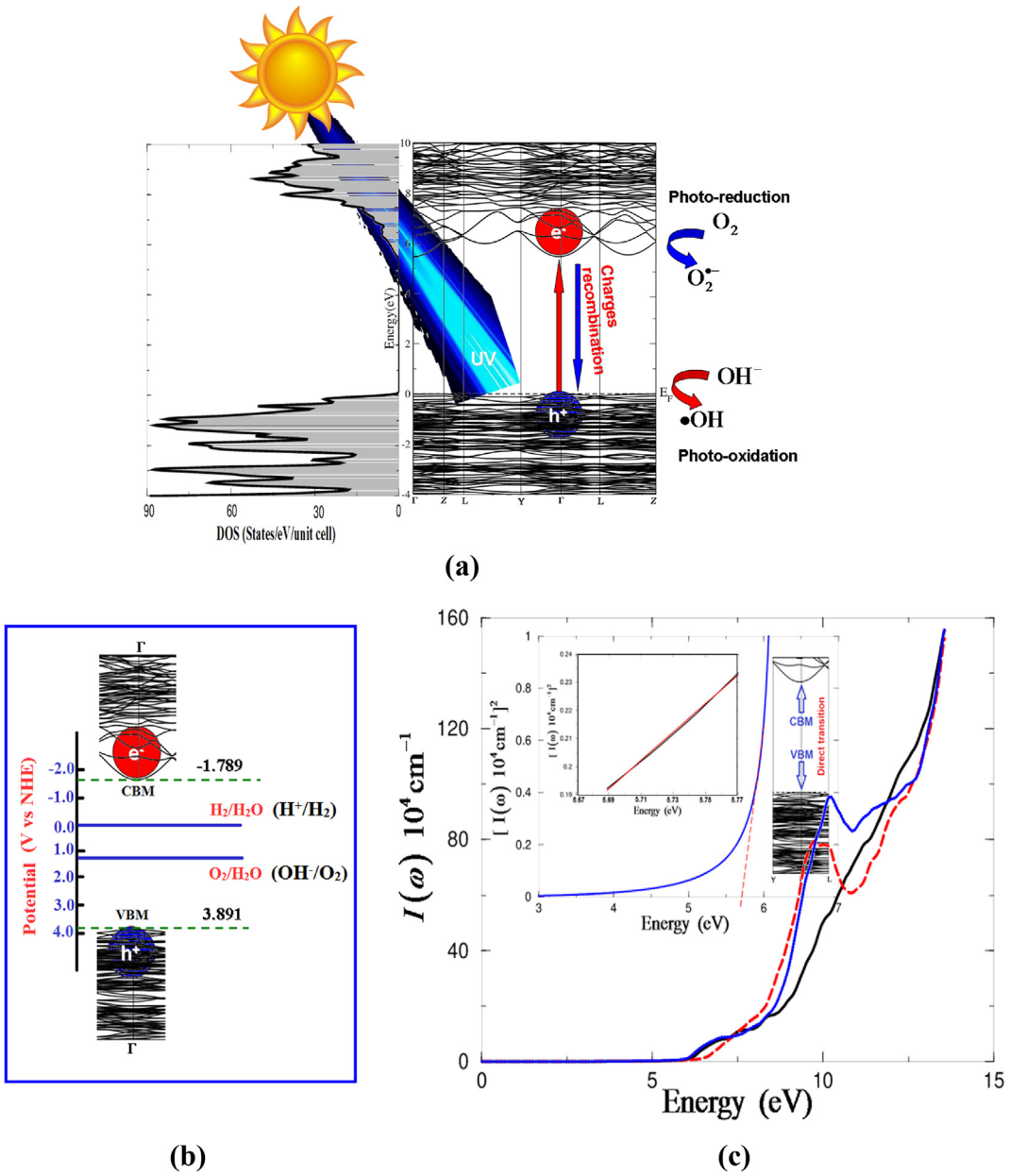

Fig. 2. (a) Schematic diagrams of charge transfer and photocatalytic mechanism of $CsZn_2B_3O_7$.; (b) potential for CBM and VBM for $CsZn_2B_3O_7$; (c) The calculated absorption spectra; (d, e) Extinction coefficient as a function of photon energy and wavelength; (f) Calculated $\sigma_2^{xx}(\omega)$ (dark solid curve-black color online),$\sigma_2^{yy}(\omega)$ (light dashed curve-red color online) and $\sigma_2^{zz}(\omega)$ (light dotted dashed curve -green color online) along with Calculated $\sigma_1^{xx}(\omega)$ (dark solid curve-blue color online), $\sigma_1^{yy}(\omega)$ (light dashed curve-red brown online) and $\sigma_1^{zz}(\omega)$ (light solid curve - violet color online). (For interpretation of the references to color in this figure legend, the reader is referred to the Web version of this article.)

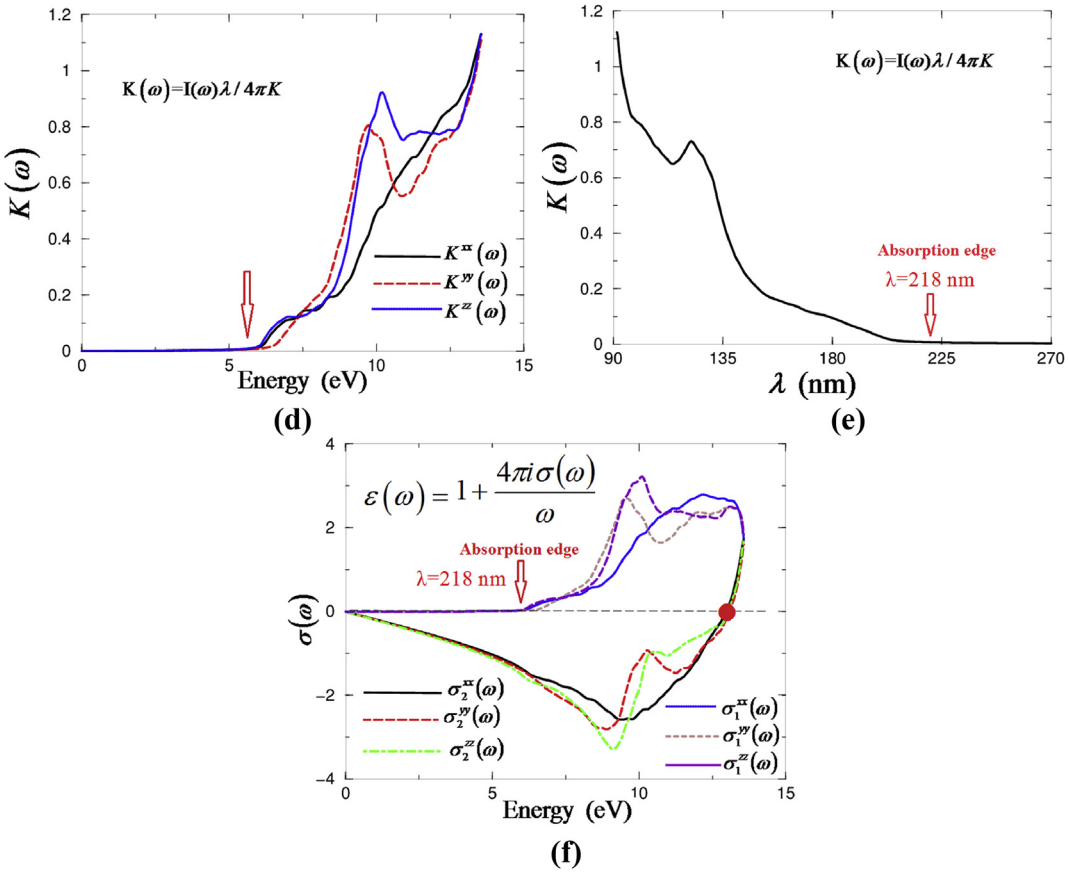

Fig. 2. (*continued*).

presence of the distorted $(ZnO_4)^{6-}$ tetrahedral, which opens the ability to safely grow crystals and increase the efficiency of the optical response almost to double in borate crystals in the UV region. Therefore, based on these promising results, one can conclude that the $CsZn_2B_3O_7$ possesses great efficiency of light-driven photocatalytic H_2 production.

3.2. Photoelectrochemical properties

The charge transfer and photocatalytic mechanism in $CsZn_2B_3O_7$ can be explained as follows: when a photocatalyst absorbs radiation from sunlight, it produces $e^- - h^+$ pairs. The electron of VB becomes excited when illuminated by light. The excess energy of this excited electron promotes the electron to the CB, therefore creating $e^- - h^+$ pairs. This stage is referred to as the semiconductor's 'photo-excitation' state. To further understand the photocatalytic mechanism in $CsZn_2B_3O_7$, the influence of the temperature (T) on the carriers' concentration (n) of $CsZn_2B_3O_7$ at a certain value of the chemical potential ($\mu = E_F$) is investigated, as shown in Fig. 3(a). It was found that n almost linearly increases with increasing T, and the positive sign indicates that the $CsZn_2B_3O_7$ exhibits p-type conductions. Furthermore, the carriers' concentration in the vicinity of E_F at three T values is investigated, as shown in Fig. 3(b). It was noticed that the difference between chemical potential (μ) and Fermi energy (E_F) is positive for VBs and negative for CBs, and $CsZn_2B_3O_7$ exhibits a maximal n in the vicinity of E_F.

For an efficient photocatalytic mechanism, a material with high mobility carriers is required. To achieve this, a material with small effective masses (m^*) is needed. It was noticed from the electronic band structure of $CsZn_2B_3O_7$ Fig. 2(a) that the high k- dispersion bands around E_F possess low m^* and, hence, the high mobility carriers (Table 1) favor the enhancement of the charge transfer process. It is well known that the m^* provides essential information to understand the photocatalytic mechanism. The mobility of the photogenerated carriers significantly influences the photocatalytic efficiency [60,61] and the higher photogenerated carriers' mobility enhances the photocatalytic performance [26,62–64]. Moreover, the great effective mass difference ($D = m_h^*/m_e^*$ and $D = m_e^*/m_h^*$) between e^- and h^+ (Table 1) can facilitate the e^- and h^+ migration and separation, and finally improve the photocatalytic performance [26,63,64]. The effective mass of e^- is bigger than that of the h^+, resulting in a significant difference in the mobility between e^- and h^+. Therefore, the mobility of e^- is much higher than that of h^+, which consequently results in a striking difference in the mobility between the photoexcited e^- and h^+. This characteristic is beneficial in suppressing the recombination of the $e^- - h^+$ pairs and improving the photocatalytic efficiency [26,63,64]. The mobility of photoexcited carriers can be indirectly assessed by their effective mass ($(mobility)_e = e\tau_e/m_e^*$ and $(mobility)_h = e\tau_h/m_h^*$). The large mobility difference is useful to the separation of e^- and h^+, the reduction of the e^- and h^+ recombination rate, and improvement of the photocatalytic activity. It is clear from Table 1 that the effective masses of the e^- and h^+ are small, and thus, we can deduce that the photogenerated carrier transfer can be fast along different directions. Fig. 3(c) shows the carriers' mobility as a function of n, which clearly shows a significant reduction in the carriers' mobility with increasing n, due to increasing the scattering. To support this statement, we investigated the carriers' mobility as a function of temperature, as shown in Fig. 3(d). It clearly shows a significant reduction in the carriers' mobility with increasing the temperature,

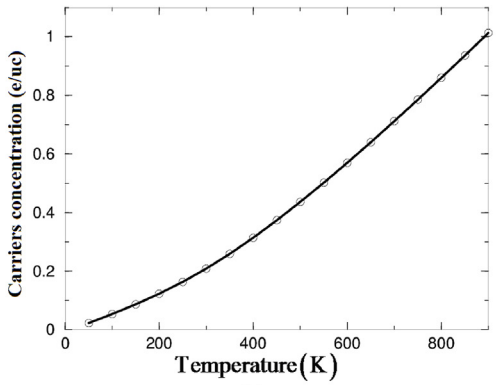

(a)

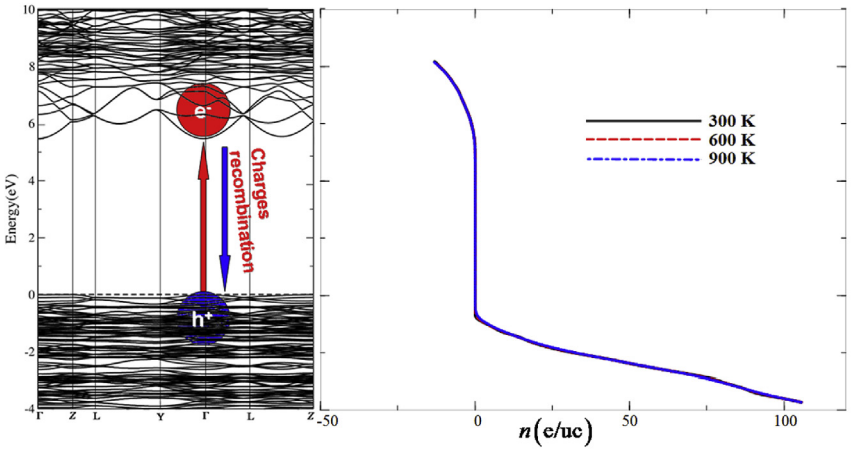

(b)

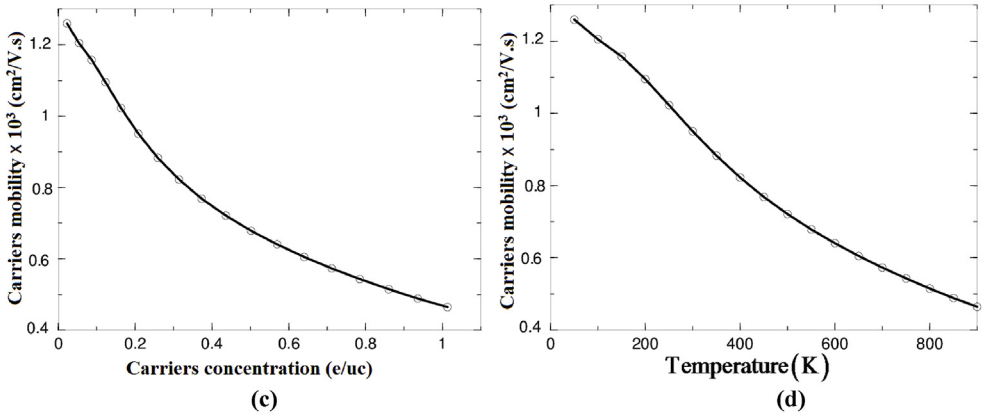

(c) (d)

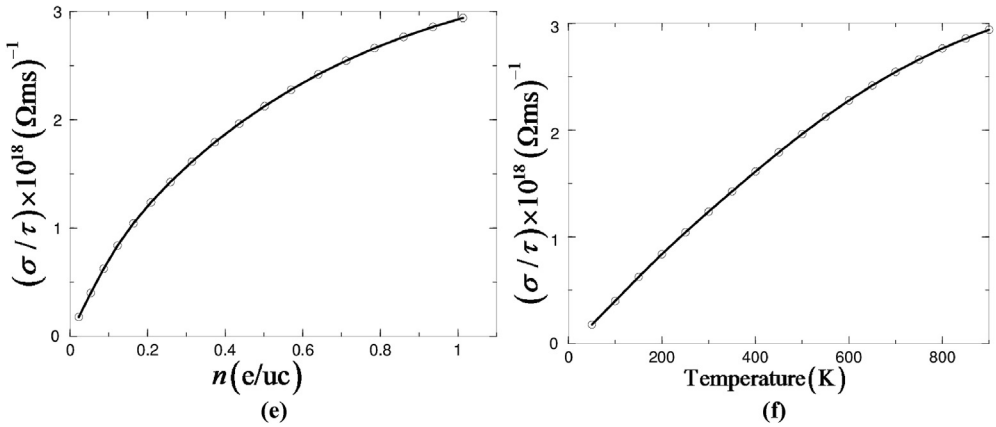

(e) (f)

Fig. 3. (a) The carrier concentration of $CsZn_2B_3O_7$ as function of temperature; (b) The carrier concentration of $CsZn_2B_3O_7$ as function of chemical potential $\mu - E_F$ at room temperature and other two randomly selected temperature; (c) the mobility of $CsZn_2B_3O_7$ s a function of carrier concentration; (e) the mobility of $CsZn_2B_3O_7$ as a function of temperature; (e) the electronic conductivity of $CsZn_2B_3O_7$ s a function of carrier concentration; (f) the electronic conductivity of $CsZn_2B_3O_7$ as a function of temperature.

Table 1
Calculated effective masses of $CsZn_2B_3O_7$.

Effective mass	
m_e^*/m_o	0.01013
m_{hh}^*/m_o	0.08448
$D = m_{hh}^*/m_e^*$	8.33958
$D = m_e^*/m_{hh}^*$	0.11991

which is attributed to the fact that raising the temperature causes an increase in the vibration and, hence, the mobility resulting in an increase in the scattering, which leads to suppression of the mobility.

The other important factor to improve the photocatalytic performance is the electronic conductivity (σ/τ) of the photogenerated carriers; therefore, the materials should possess high σ/τ. It is well known that σ/τ is directly related to the charge carriers' concentration and their mobility $(\sigma/\tau = ne\eta)$; here we call the mobility η in order to distinguish between the mobility and chemical potential (μ). Since $CsZn_2B_3O_7$ possesses high mobility and high carrier concentration, one expects that $CsZn_2B_3O_7$ will exhibit high σ/τ. To verify this, the σ/τ as a function of n is shown in Fig. 3(e). It has been found that σ/τ increases with increasing n. Furthermore, the σ/τ as a function of temperature is plotted in Fig. 3(f), which shows that σ/τ increases with increasing the temperature. Following Fig. 3(e and f), one can conclude that σ/τ significantly depends on the temperature and n. Therefore, the photogenerated carriers in $CsZn_2B_3O_7$ possess high electronic conductivity, favoring enhancement of the photocatalytic efficiency.

Further understanding of the photocatalytic mechanism in $CsZn_2B_3O_7$, can be gained from the angular momentum projected density of states, as shown in Fig. 4(a–d). The angular momentum projected density of states shows that the electronic structure exhibits highly dispersive CB and VB which provide favorable support to facilitate the transport of photoinduced charge carriers. This is considered a significant process for photocatalysis. Furthermore, it shows the direct band gap nature, since the TVB and the BCB are situated at Γ point of the BZ. The TVB is composed of Zn-3d, and O-2p, with a small contribution from Zn-4s/3p states. It is clear that the Zn-3d state is responsible for constructing the TVB, which could induce relatively localized photoholes. The BCB is mainly formed by the Zn-4s state, while Cs-6s and O-2s states contribute little to the composition of the BCB. This implies that the presence of the distorted $(ZnO_4)^{6-}$ tetrahedra cause a significant band gap reduction towards the UV region. Thus, separate occupation of the orbitals from cationic and anionic layers in the CB and VB favors separation of the photogenerated $e^- - h^+$. The angular momentum projected density of states reveals the hybridization between the states; for instance, Zn-3d strongly hybridized with the O-2p state, the O-2p state hybridizes with Cs-4d, Zn-4s with the O-2s, Zn-3p and B-2s/

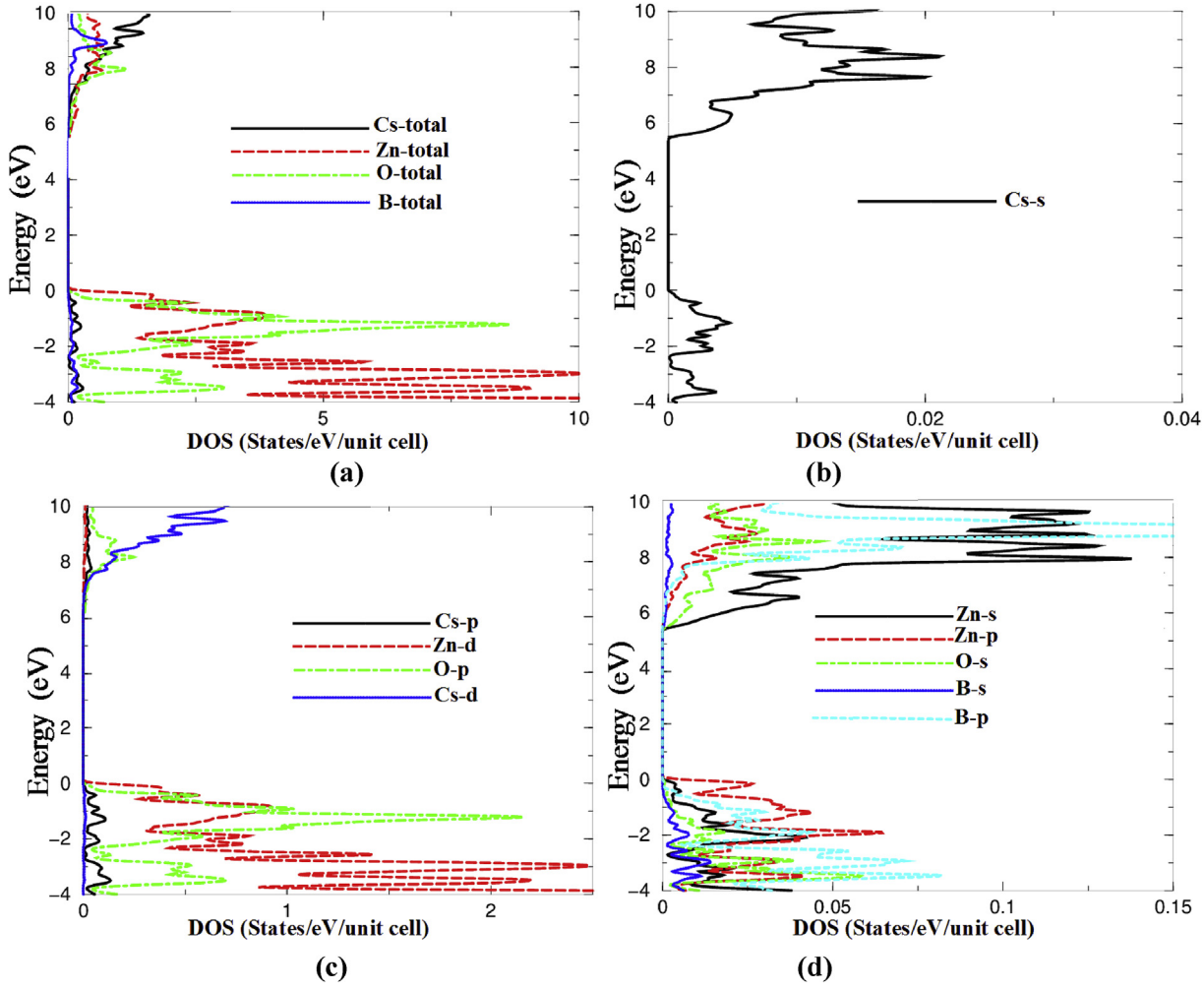

Fig. 4. (a–d) The projected density of states along with the angular momentum character of various structures of $CsZn_2B_3O_7$.

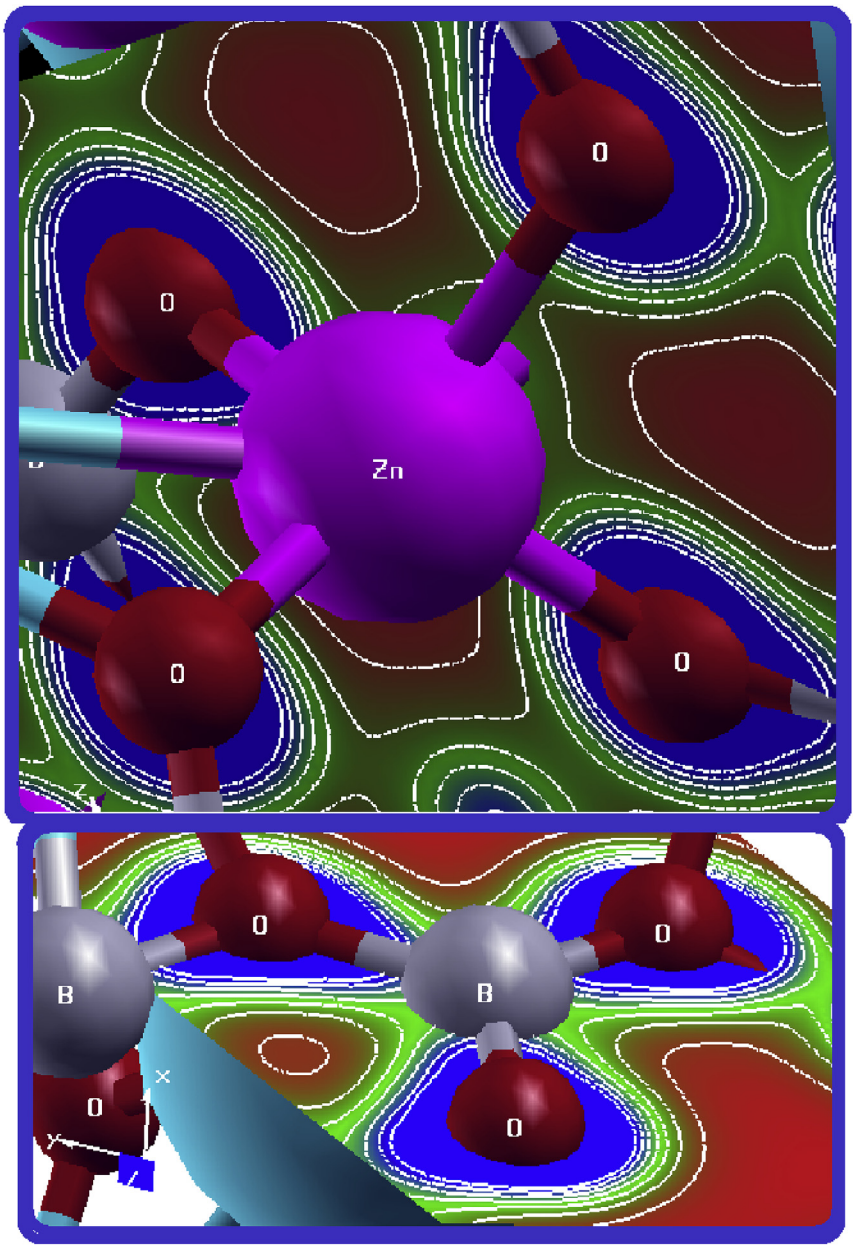

(a)

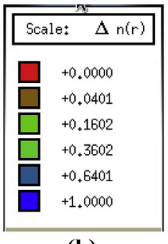

(b)

Fig. 5. (a) The electron cloud of the BO_3 anionic groups which exhibit planar shape with conjugated electron orbitals which make the BO_3 anionic groups are the main source of the large birefringence in $CsZn_2B_3O_7$. The electron cloud of the distorted $(ZnO_4)^{6-}$ tetrahedra. (b) thermoscale show the blue color indicates the maximum charge intensity (1.0000). (For interpretation of the references to color in this figure legend, the reader is referred to the Web version of this article.)

Table 2
The calculated values of the ionic character.

Bonds	P (%)
B–O	29.26
Zn–O	39.85
Cs–B	26.46
Cs–O	68.36
Cs–Zn	17.23

2p states. The hybridization may lead to the formation of covalent bonding depending on the degree of the hybridization, which is more favorable for the transport of the carriers than an ionic bonding [65].

To support this statement and in order to reveal the chemical bonding nature of $CsZn_2B_3O_7$, the electronic charge density distribution is calculated in two crystallographic planes: (1 0 0) and (1 0 1), as shown in Fig. 5. The charge localizes mainly between Zn and the neighboring O atoms in ZnO_4 tetrahedra, also between B and O atoms in the co-parallel BO_3 triangle groups, indicating a partial ionic and strong covalent bonding. The strength of the interactions between the atoms is due to the degree of the hybridization and the electronegativity differences. According to the Pauling scale, the electronegativity of Cs, Zn, B and O are 0.75, 1.65, 2.04 and 3.44, respectively. To describe the character of the chemical bonding in $CsZn_2B_3O_7$, the difference of the electronegativity (X_A–X_B) is crucial [66], where X_A and X_B denote the electronegativity of the A and B atoms in general. With an increase in the (X_A–X_B) difference, the ionic character (P) of the bonding increases. The percentage of P for the chemical bonding can be obtained using the expression [66]:

$$P(\%) = 16(X_A - X_B) + 3.5(X_A - X_B)^2. \quad (5)$$

The calculated values of P are given in Table 2. It is clear that the Zn–O and B–O bonds are mostly covalent and partially ionic bonding. The covalent bonding is more favorable for the transport of the carriers than ionic bonding [65]. Also, due to the electronegativity differences between the atoms, some valence electrons are transferred to O atoms, as it is clear that these atoms are surrounded by uniform blue spheres which indicate the maximum charge accumulation according to the thermoscale Fig. 5(b). The Zn–O and B–O units possess strong electron cloud overlap and prefer to attract holes and repel electrons, thus facilitating separation of the photogenerated $e^- - h^+$ pairs. This in turn enhances the photocatalytic activity [4].

Electronegativity is probably the most important concept to understand the inorganic chemistry. Electronegativity refers to the power of an atom in a molecule to attract electrons to itself. If the Zn, B and O atoms are compared in terms of electronegativity, the oxygen is more electronegative than Zn and B; thus, oxygen has greater power to attract electrons to itself than Zn and B do. If one thinks about the electrons and the covalent bonds between B and O that are shared, they are shared unequally due the fact that O is more electronegative and, thus, it pulls the electrons closer to itself and becomes more negatively charged, and B loses some electrons and electron density. Therefore, B is partially positive and O is partially negative; that is a polarized situation and since the electronegativity difference between B and O is less than 1.7 [64], it is a polar covalent bond. In contrast, for Zn and O the electronegativity difference is 1.79; therefore, it is a polar ionic bond.

4. Conclusions

An ab-initio calculation utilizing the full-potential method is used to investigate the photocatalytic performance of the novel borate $CsZn_2B_3O_7$. The calculation highlights that: (i) the potentials of CB and VB edge values of $CsZn_2B_3O_7$ are −1.789 eV and 3.891 eV. Thus, the CB edge potential of $CsZn_2B_3O_7$ is more negative than the redox potential of H^+/H_2, indicating that the $CsZn_2B_3O_7$ has strong reduction power for H_2 production. (ii) the absorption edge of $CsZn_2B_3O_7$ occurs in the UV region with strong absorption of about $10^4\,cm^{-1}$. Thus, $CsZn_2B_3O_7$ possesses an appropriate band gap width and suitable CB edge position together, which leads to a higher efficiency of light-driven photocatalytic H_2 production. It also possesses high photogenerated carrier mobility and high electronic conductivity, favoring the enhancement of the photocatalytic performance. (iii) efficient separation and migration ability of the photoexcited carriers, due to the fact that the photocatalytic reaction utilizes the photoexcited e^- and h^+ migrating to the surface of the photocatalyst. (iv) the packing of the BO_3 structural unit is the main source for the high macroscopic photophysical properties in $CsZn_2B_3O_7$ due to high anisotropic electron distribution. The high photocatalytic performance is due to the strong interactions between the ZnO_4 tetrahedra and co-parallel BO_3 triangle groups. The absorption edge of $CsZn_2B_3O_7$ occurs at $\lambda = 218$ nm and the optical band gap is estimated to be 5.68 eV, in good agreement with the experimental data (5.69 eV). Therefore, based on these results, one can conclude that $CsZn_2B_3O_7$ possess appropriate band gap width and satisfies all requirements to be an efficient photocatalyst. This will greatly improve the search efficiency and greatly help experiments to save resources in the exploration of new photocatalysts with good photocatalytic performance.

Acknowledgments

The result was developed within the CENTEM project, reg. no. CZ.1.05/2.1.00/03.0088, cofunded by the ERDF as part of the Ministry of Education, Youth and Sports OP RDI programme and, in the follow-up sustainability stage, supported through CENTEM PLUS (LO1402) by financial means from the Ministry of Education, Youth and Sports under the “National Sustainability Programme I”. Computational resources were provided by MetaCentrum (LM2010005) and CERIT-SC (CZ.1.05/3.2.00/08.0144) infrastructures.

Appendix A. Supplementary data

Supplementary data related to this article can be found at https://doi.org/10.1016/j.jallcom.2018.01.227.

References

[1] M. Muruganandham, R. Amutha, G.J. Lee, S.H. Hsieh, J.J. Wu, M. Sillanpaa, Facile fabrication of tunable Bi_2O_3 self-assembly and its visible light photocatalytic activity, J. Phys. Chem. C 116 (2012) 12906–12915.
[2] L. Huang, X.L. Wang, J.H. Yang, G. Liu, J.F. Han, C. Li, Dual cocatalysts loaded type I CdS/ZnS core/shell nanocrystals as effective and stable photocatalysts for H_2 evolution, J. Phys. Chem. C 117 (2013) 11584–11591.
[3] T. Wen, D.X. Zhang, J. Zhang, Two-dimensional copper(I) coordination polymer materials as photocatalysts for the degradation of organic dyes, Inorg. Chem. 52 (2013) 12–14.
[4] X. Fan, L. Zang, M. Zhang, H. Qiu, Z. Wang, J. Yin, H. Jia, S. Pan, C. Wang, A bulk boron-based photocatalyst for efficient dechlorination: $K_3B_6O_{10}Br$, Chem. Mater. 26 (2014) 3169–3174.
[5] H. Tong, S.X. Ouyang, Y.P. Bi, N. Umezawa, M. Oshikiri, J.H. Ye, Nano-photocatalytic materials: possibilities and challenges, Adv. Mater. 24 (2012) 229–251.
[6] Y. Yang, X. Jiang, Z. Lin, Y. Wu, Borate-based ultraviolet and deep-ultraviolet nonlinear optical crystals, Crystals 7 (2017) 95.
[7] C.T. Chen, T. Sasaki, R. Li, Y. Wu, Z. Lin, Y. Mori, Z. Hu, J. Wang, G. Aka, M. Yoshimura, Y. Kaneda, Nonlinear Optical Borate Crystals Principals and Applications, Wiley-VCH, New York, NY, USA, 2012, ISBN 978-3-527-41009-5.
[8] H. Yu, H. Wu, S. Pan, Z. Yang, X. Hou, X. Su, Q. Jing, K.R. Poeppelmeier, J.M. Rondinelli, $Cs_3Zn_6B_9O_{21}$: a chemically benign member of the KBBF family

exhibiting the largest second harmonic generation response, J. Am. Chem. Soc. 136 (2014) 1264–1267.
[9] C.T. Chen, J.H. Lu, T. Togashi, T. Suganuma, T. Sekikawa, S. Watanabe, Z.Y. Xu, J.Y. Wang, Second-harmonic generation from a $KBe_2BO_3F_2$ crystal in the deep ultraviolet, Opt. Lett. 27 (2002) 637–639.
[10] B.C. Wu, D.Y. Tang, N. Ye, C.T. Chen, Linear and nonlinear optical properties of the KBe2BO3F2 crystal, Opt. Mater. 5 (1996) 105–109.
[11] C.T. Chen, G.L. Wang, X.Y. Wang, Z.Y. Xu, Deep-UV nonlinear optical crystal $KBe_2BO_3F_2$ discovery, growth, optical properties and applications, Appl. Phys. B 97 (2009) 9–25.
[12] M. Abudoureheman, L. Wang, X. Zhang, H. Yu, Z. Yang, C. Lei, J. Han, S. Pan, $Pb_7O(OH)_3(CO_3)_3(BO_3)$: first mixed borate and carbonate nonlinear optical material exhibiting large second-harmonic generation response, Inorg. Chem. 54 (2015) 4138–4142.
[13] Z. Lin, X. Jiang, L. Kang, P. Gong, S. Luo, M.-H. Lee, First-principles materials applications and design of nonlinear optical crystals, J. Phys. D Appl. Phys. 47 (2014), 253001.
[14] L. Liu, Y. Yang, X. Dong, B. Zhang, Y. Wang, Z. Yang, S. Pan, Design and syntheses of three novel carbonate halides: $Cs_3Pb_2(CO_3)_3I$, $KBa_2(CO_3)_2F$, and $RbBa_2(CO_3)_2F$, Chem. Eur J. 22 (2016) 2944–2954.
[15] G.E. Davydyuk, O.Y. Khyzhun, A.H. Reshak, H. Kamarudin, G.L. Myronchuk, S.P. Danylchuk, A.O. Fedorchuk, L.V. Piskach, M. Yu. Mozolyuk, O.V. Parasyuk, Photoelectrical properties and the electronic structure of $Tl_{1-x}In_{1-x}Sn_xSe_2$ (x = 0, 0.1, 0.2, 0.25) single crystalline alloys, Phys. Chem. Chem. Phys. 15 (2013) 6965.
[16] A.H. Reshak, Y.M. Kogut, A.O. Fedorchuk, O.V. Zamuruyeva, G.L. Myronchuk, O.V. Parasyuk, H. Kamarudin, S. Auluck, K.L. Plucinskig, J. Bila, Linear, nonlinear optical susceptibilities and the hyperpolarizability of the mixed crystals $Ag_{0.5}Pb_{1.75}Ge(S_{1-x}Se_x)_4$: experiment and theory, Phys. Chem. Chem. Phys. 15 (2013) 18979.
[17] S.F. Solodovnikov, V.V. Atuchin, Z.A. Solodovnikova, O.Y. Khyzhun, M.I. Danylenko, D.P. Pishchur, P.E. Plyusnin, A.M. Pugachev, T.A. Gavrilova, A.P. Yelisseyev, A.H. Reshak, Z.A. Alahmed, N.F. Habubi, Synthesis, structural, thermal, and electronic properties of palmierite-related double molybdate α-Cs2Pb(MoO4)2, Inorg. Chem. 56 (2017) 3276–3286.
[18] O.Y. Khyzhun, V.L. Bekenev, V.V. Atuchin, L.D. Pokrovsky, V.N. Shlegel, N.V. Ivannikova, The electronic structure of Pb2MoO5: first-principles DFT calculations and X-ray spectroscopy measurements, Mater. Des. 105 (2016) 315–322.
[19] O.Y. Khyzhun, V.L. Bekenev, V.V. Atuchin, E.N. Galashov, V.N. Shlegel, Electronic properties of ZnWO4 based on ab initio FP-LAPW band-structure calculations and X-ray spectroscopy data, Mater. Chem. Phys. 140 (2013) 558–595.
[20] V.V. Atuchin, E.N. Galashov, O.Y. Khyzhun, V.L. Bekenev, L.D. Pokrovsky, Yu. A. Borovlev, V.N. Zhdankov, Low thermal gradient Czochralski growth of large $CdWO_4$ crystals and electronic properties of (010) cleaved surface, J. Solid State Chem. 236 (2016) 24–31.
[21] H. Huang, X. Li, J. Wang, F. Dong, P.K. Chu, T. Zhang, Y. Zhang, Anionic group self-doping as a promising strategy: band-gap engineering and multifunctional applications of high-performance CO_3^{2-}-doped $Bi_2O_2CO_3$, ACS Catal. 5 (2015) 4094–4103.
[22] H. Huang, X. Han, X. Li, S. Wang, P.K. Chu, Y. Zhang, Fabrication of multiple heterojunctions with tunable visible-light-active photocatalytic reactivity in BiOBr–BiOI full-range composites based on microstructure modulation and band structures, ACS Appl. Mater. Interfaces 7 (2015) 482–492.
[23] H. Huang, Y. He, X. Li, M. Li, C. Zeng, F. Dong, X. Du, T. Zhangd, Y. Zhang, $Bi_2O_2(OH)(NO_3)$ as a desirable $[Bi_2O_2]^{2+}$ layered photocatalyst: strong intrinsic polarity, rational band structure and {001} active facets co-beneficial for robust photooxidation capability, J. Mater. Chem. A 3 (2015) 24547–24556.
[24] H. Huang, Y. He, Z. Lin, L. Kang, Y. Zhang, Two novel Bi-based borate photocatalysts: crystal structure, electronic structure, photoelectrochemical properties, and photocatalytic activity under simulated solar light irradiation, J. Phys. Chem. C 117 (2013) 22986–22994.
[25] J. Zhang, W. Yu, J. Liu, B. Liud, Illustration of high-active Ag2CrO4 photocatalyst from the first-principle calculation of electronic structures and carrier effective mass, Appl. Surf. Sci. 358 (2015) 457–462.
[26] X. Li, J. Zhao, J. Yang, Semihydrogenated BN sheet: a promising visible-light driven photocatalyst for water splitting,, Sci. Rep. 3 (2013) 1858.
[27] H. Zhang, L. Liua, Z. Zhou, Towards better photocatalysts: first-principles studies of the alloying effects on the photocatalytic activities of bismuth oxyhalides under visible light, Phys. Chem. Chem. Phys. 14 (2012) 1286–1292.
[28] C. Liu, Y. Zhang, F. Dong, A.H. Reshak, L. Ye, N. Pinna, C. Zeng, T. Zhang, H. Huang, Chlorine intercalation in graphitic carbon nitride for efficient photocatalysis, Appl. Catal. B Environ. 203 (2017) 465–474.
[29] H. Huang, S. Tu, C. Zeng, T. Zhang, A.H. Reshak, Y. Zhang, Polarization enhancement promoting photo- and piezoelectric-induced charge separation and molecular oxygen activation, Angew. Chem. Int. Ed. 56 (2017) 11860–11864.
[30] A.H. Reshak, Active photocatalytic water splitting solar-to-hydrogen energy conversion: chalcogenide photocatalyst Ba_2ZnSe_3 under visible irradiation, Appl. Catal. B Environ. 221 (2018) 17–26.
[31] A.H. Reshak, Quantum dots in photocatalytic applications: efficiently enhancing visible light photocatalytic activity by integrating CdO quantum dots as sensitizer, Phys. Chem. Chem. Phys. 19 (2017) 24915.
[32] A.H. Reshak, Photocatalytic water splitting solar-to-hydrogen energy conversion: perovskite-type hydride XBeH3 (X = Li or Na) as active photocatalysts, J. Catal. 351 (2017) 119–129.
[33] A.H. Reshak, Photophysical, transport and structure properties of Tl10Hg3Cl16 single crystals: novel photocatalytic water-splitting solar-to-hydrogen energy conversion, J. Catal. 352 (2017) 142–154.
[34] A.H. Reshak, S. Auluck, Photocatalytic water-splitting solar-to-hydrogen energy conversion: novel LiMoO3(IO3) molybdenyl iodate based on WO3-type sheets, J. Catal. 351 (2017) 1–9.
[35] S. Zhao, J. Zhang, S.Q. Zhang, Z. Sun, Z. Lin, Y. Wu, M. Hong, J. Luo, A new UV nonlinear optical material $CsZn_2B_3O_7$: ZnO_4 tetrahedra double the efficiency of second-harmonic generation, J. Inorg. Chem. 53 (2014) 2521–2527.
[36] C.T. Chen, Y.B. Wang, B.C. Wu, K. Wu, W. Zeng, L.H. Yu, Design and synthesis of an ultraviolet-transparent nonlinear optical crystal $Sr_2Be_2B_2O_7$, Nature 373 (1995) 322–324.
[37] N. Ye, W.R. Zeng, J. Jiang, B.C. Wu, C.T. Chen, B.H. Feng, X.L. Zhang, New nonlinear optical crystal $K_2Al_2B_2O_7$, Opt. Soc. Am. B 17 (2000) 764.
[38] S.C. Wang, N. Ye, W. Li, D. Zhao, Alkaline beryllium borate $NaBeB_3O_6$ and $ABe_2B_3O_7$ (A = K, Rb) as UV nonlinear optical crystals, J. Am. Chem. Soc. 132 (2010) 8779–8786.
[39] J. Jiang, X. Zhang, P.B. Sun, L.Z. Zhang, ZnO/BiOI heterostructures: photoinduced charge-transfer property and enhanced visible-light photocatalytic activity, J. Phys. Chem. C 115 (2011) 20555–20564.
[40] P. Blaha, K. Schwarz, G.K.H. Madsen, D. Kvasnicka, J. Luitz, WIEN2k, an Augmented Plane Wave Plus Local Orbitals Program for Calculating Crystal Properties, Vienna University of Technology, Austria, 2001.
[41] J.P. Perdew, S. Burke, M. Ernzerhof, Generalized gradient approximation made simple, Phys. Rev. Lett. 77 (1996) 3865.
[42] F. Tran, P. Blaha, Accurate band gaps of semiconductors and insulators with a semilocal exchange-correlation potential, Phys. Rev. Lett. 102 (2009), 226401.
[43] T. Goldacker, V. Abetz, R. Stadler, I. Erukhimovich, L. Leibler, Non-centrosymmetric superlattices in block copolymer blends, Nature 398 (1999) 137.
[44] M. Stock, S. Dunn, Influence of the ferroelectric nature of lithium niobate to drive photocatalytic dye decolorization under artificial solar light, J. Phys. Chem. C 116 (2012) 20854–20859.
[45] Y. Cui, J. Briscoe, S. Dunn, Effect of ferroelectricity on solar-light-driven photocatalytic activity of $BaTiO_3$—influence on the carrier separation and stern layer formation, Chem. Mater. 25 (2013) 4215–4223.
[46] S.V. Kalinin, D.A. Bonnell, Nanoscale Phenomena in Ferroelectric Thin Films, Kluwer Academic Publications, Dordrecht, The Netherlands, 2004, pp. 182–216.
[47] S. Dunn, P.M. Jones, D.E. Gallardo, Photochemical growth of silver nanoparticles on c^- and c^+ domains on lead zirconate titanate thin films, J. Am. Chem. Soc. 129 (2007) 8724.
[48] Y. Inoue, K. Sato, K. Sato, H. Miyama, Photoassisted water decomposition by ferroelectric lead zirconate titanate ceramics with anomalous photovoltaic effects, J. Phys. Chem. 90 (1986) 2809.
[49] L. Li, P.A. Salvador, G.S. Rohrer, Photocatalysts with internal electric fields, Nanoscale 6 (2014) 24.
[50] M.E. Lines, A.M. Glass, Principles and Applications of Ferroelectrics and Related Materials, Clarendon Press, Oxford, U.K., 2001.
[51] C.T. Chen, Z.S. Lin, Z.Z. Wang, The development of new borate-based UV nonlinear optical crystals, Appl. Phys. B Laser Opt. 80 (2005) 1–25.
[52] M.T. Buelow, A.J. Gellman, The transition state for metal catalyzed dehalogenation: C-I bond cleavage on Ag(111), J. Am. Chem. Soc. 123 (2001) 1440–1448.
[53] P. Zhou, J.H. Wu, W.L. Yu, G.H. Zhao, G.J. Fang, S.W. Cao, Vectorial doping-promoting charge transfer in anatase TiO2 {0 0 1} surface, Appl. Surf. Sci. 319 (2014) 167–172.
[54] P.J. Zhou, G. Yu, M. Jaroniec, All-solid-state Z-scheme photocatalytic systems, Adv. Mater. 26 (2014) 4920–4935.
[55] Q. Li, H. Meng, P. Zhou, Y.Q. Zheng, J. Wang, J.G. Yu, J.R. Gong, $Zn_{1-x}Cd_xS$ solid solutions with controlled bandgap and enhanced visible-light photocatalytic H_2-production activity, ACS Catal. 3 (2013) 882–889.
[56] X. Chang, T. Wang, J. Gong, CO_2 photo-reduction: insights into CO_2 activation and reaction on surfaces of photocatalysts, J. Energy Environ. Sci. 9 (2016) 2177–2196.
[57] J. Dalal, N. Sinha, B. Kumar, Structural, optical and dielectric studies of novel non-linear bisglycine lithium nitrate piezoelectric single crystal, Opt. Mater. 37 (2014) 457–463.
[58] F. Bassani, G.P. Parravicini, Electronic States and Optical Transitions in Solids, Pergamon Press Ltd., Oxford, 1975, pp. p149–154.
[59] C. Ambrosch-Draxl, J.O. Sofo, Linear optical properties of solids within the full-potential linearized augmented planewave method, Comput. Phys. Commun. 175 (2006) 1–14.
[60] J.W. Tang, J.H. Ye, Photocatalytic and photophysical properties of visible-light-driven photocatalyst $ZnBi_{12}O_{20}$, Chem. Phys. Lett. 410 (2005) 104–107.
[61] T.L. Bahers, M. Rerat, P. Sautet, Semiconductors used in photovoltaic and photocatalytic devices: assessing fundamental properties from DFT, J. Phys. Chem. C 118 (2014) 5997–6008.
[62] J. Sato, H. Kobayashi, Y. Inoue, Photocatalytic activity for water decomposition of indates with octahedrally coordinated d^{10} configuration. II. roles of geometric and electronic structures, J. Phys. Chem. B 107 (2003) 7970–7975.
[63] J.F. Zhang, P. Zhou, J.J. Liu, J.G. Yu, New understanding of the difference of

photocatalytic activity among anatase, rutile and brookite TiO_2, Phys. Chem. Chem. Phys. 16 (2014) 20382–20386.
[64] J. Yang, P. Jiang, M. Yue, D. Yang, R. Cong, W. Gao, T. Yang, $Bi_2Ga_4O_9$: an undoped single-phase photocatalyst for overall water splitting under visible light, J. Catal. 345 (2017) 236–244.
[65] F. Wu, H.Z. Song, J.F. Jia, X. Hu, Effects of Ce, Y, and Sm doping on the thermoelectric properties of Bi_2Te_3 alloy, Prog. Nat. Sci. Mater. Int. 23 (2013) 408–412.
[66] 41st IFF Spring schoolSchlusseltechnologien Key Technologies, 11, 2010, ISBN 978-3-89336-559-3. pp A1–18.